



# Photoelectrochemical properties of doped TiO<sub>2</sub> nanowires grown by seed-assisted thermal oxidation

Massimo Zimbone<sup>1</sup>, Sergio Battiato<sup>1,2,\*</sup>, Lucia Calcagno<sup>2</sup>, Gianni Pezzotti Escobar<sup>1</sup>,  
Giovanna Pellegrino<sup>1</sup>, Salvo Mirabella<sup>1,2</sup>, Federico Giuffrida<sup>2</sup>, and Giuliana Impellizzeri<sup>1</sup>

<sup>1</sup> CNR-IMM, Via S. Sofia 64, 95123 Catania, Italy

<sup>2</sup> Department of Physics and Astronomy, University of Catania, Via S. Sofia 64, 95123 Catania, Italy

Received: 24 January 2024

Accepted: 10 May 2024

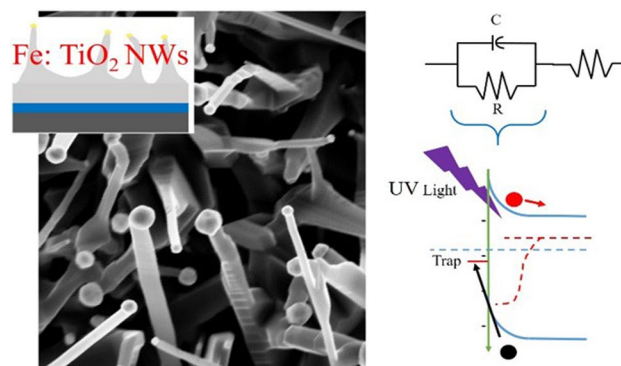
Published online:  
28 May 2024

© The Author(s), 2024

## ABSTRACT

Titanium dioxide Nanowires (NWs) are particularly interesting because of their very high surface/volume ratio and their photocatalytic activity allows them to be used in a myriad of applications. This manuscript presents a study of nanowires grown on a conductive substrate making use of a seed-assisted thermal oxidation process. To obtain doped NWs, before the oxidation, metallic titanium was doped with Fe (or Cr) by ion implantation technology. Analyses showed good quality Rutile phase and light absorption in the visible range. Transport properties of the NWs/electrolyte junction were investigated by using linear sweep voltammetry and electrochemical impedance spectroscopy. They allowed us to measure the photovoltage and the barrier height of the junction. We also evaluated the density of hole trap states at the interface during illumination. Electrical results indicate that the formation of deep levels, induced by doping, influences the electron concentration in the TiO<sub>2</sub> and the transport properties.

## GRAPHICAL ABSTRACT



Handling Editor: M. Grant Norton.

Address correspondence to E-mail: sergio.battiato@dfa.unict.it

<https://doi.org/10.1007/s10853-024-09763-6>

## Introduction

Titanium dioxide ( $\text{TiO}_2$ ) emerges as a compelling material, captivating attention for its remarkable properties. It has exceptional attributes, including favourable optical and electronic properties, long durability, persistent chemical stability, robust corrosion resistance, and economic affordability. This versatile material boasts a range of practical uses in photocatalysis, photovoltaics, chemical sensing, and optical devices [1, 2]. Its utility extends also to create super hydrophilic and self-cleaning surfaces [3, 4]. One of the key properties that unlock this wide range of applications is its ability to degrade organic compounds absorbed onto its surface when exposed to ultraviolet (UV) radiation [5–10]. The functionality of many of its applications hinges on the efficient transport of photo-generated electrons and holes to the external environment, enabling the degradation of absorbed pollutants on the  $\text{TiO}_2$  surface into harmless substances. In addition, it is widely acknowledged that further enhancements are needed to boost the efficiency of  $\text{TiO}_2$  photocatalysis, especially extending the range of the useful radiation to visible light. The scientific community has explored various approaches to enhance the effectiveness of this process [11–16].

Nanowires (NWs) present a particularly promising avenue for improvement [17–19]. In particular, the extremely high surface-to-volume ratio of  $\text{TiO}_2$  NWs enhances the interaction of the photo-carriers with the external environment, leading to an enhanced photocatalytic activity. In the literature, several methods for the synthesis of  $\text{TiO}_2$  NWs are reported: hydrothermal [20], chemical vapour deposition (CVD) [21], atomic layer deposition (ALD) [22], and thermal oxidation [23]. Our group has significant experience in the synthesis of titania nanowires by thermal oxidation [15, 24, 25].  $\text{TiO}_2$  NWs are grown on a titanium layer (or foil) using gold nanoparticles as seeds for the growth. Such a peculiar growth technique creates NWs with a gold nanoparticle tip. Moreover, an intimate Ohmic (non-rectifying) electrical junction between  $\text{TiO}_2$  NWs and the conductive titanium substrate is achieved allowing the electrochemical measurements to be reliable [15, 24, 25].

This is particularly interesting since Au, and in general noble metals, are commonly used to enhance the photoactivity of the  $\text{TiO}_2$  and because Au nanoparticles are easily functionalized. These facts give some

degree of freedom in the realization of devices for water purification and sensing [26–28].

While most of the literature predominantly emphasizes the photocatalytic behaviour of  $\text{TiO}_2$  NWs, the focus of this paper is to delve into understanding the photo-electrochemical peculiarities of  $\text{TiO}_2$  NWs grown by seed-assisted Au nanoparticles. This choice is motivated by the profound interconnection between photocatalytic behaviour and their electrochemical properties. After an optical, morphological and structural analysis of the NWs, we used the electrochemical impedance spectroscopy (EIS) measurements at various applied voltages together with the current–voltage (LSV, linear sweep voltammetry) characteristics to understand the physical–chemical properties of the NWs interface. We gave a rationale for the effect of the doping and for the formation of trap states for minority carriers (photo–holes) at the interface during illumination. We also studied, together with the pristine  $\text{TiO}_2$  NWs, the Cr and Fe-doped  $\text{TiO}_2$  NWs. We chose these ions because it is well known that ion doping brings a decrease in the band gap of the material and an absorption in the visible range that could enhance the photo-catalytical properties also in the visible range [29]. This study seeks to contribute valuable insights into the photo-electrochemical aspects that influence the performance of titanium dioxide in various applications.

## Materials and methods

The procedure for the synthesis of the nanowires is schematically shown in Fig. 1 and consists of several steps. For the undoped material, only 3 steps (described in Fig. 1 as steps 1, 3 and 4) are necessary, while for doped material a further step (i.e. step 2) was added as we will discuss later.

### Undoped NWs

Firstly, a thick ( $\sim 4 \mu\text{m}$ ) film of titanium was deposited by sputtering on a silicon substrate (Step 1). Samples were cut into pieces of about  $1 \text{ cm} \times 5 \text{ cm}$  and then a thin gold layer ( $\sim 5 \text{ nm}$  thick) was deposited on the surface of the Ti layer (step 3) by using an RF (60 Hz) Emitech K550X as a metallization sputtering system. The Au target had a 99.999% purity. The deposition was carried out in Ar flow at a current of 10 mA and a chamber pressure of 2 Pa (0.02 mbar). The thickness

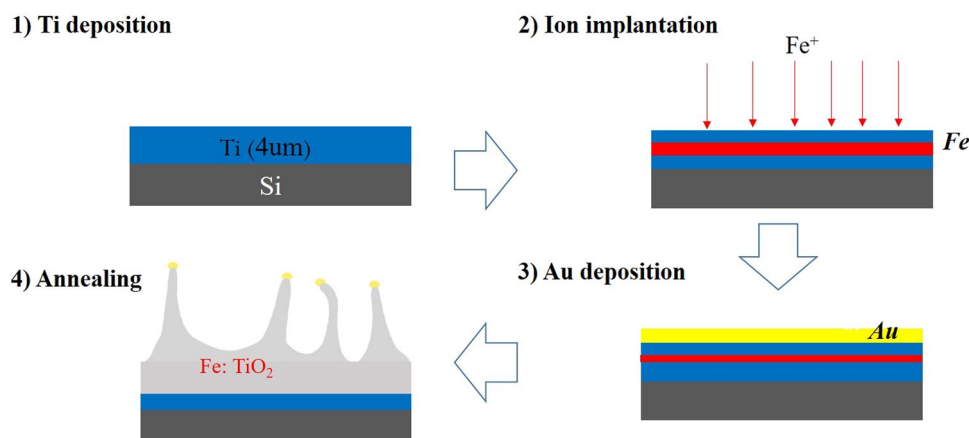


**Figure 1** A four-step procedure for the synthesis of doped NWs. Step (1) Deposition of a thick ( $\sim 4 \mu\text{m}$ ) film of titanium on a silicon substrate. Step (2) Ion implantation of the  $\text{Fe}^+$  or  $\text{Cr}^+$  ions at about 100 nm above the titanium surface. Step (3) Deposition

a thin gold layer ( $\sim 5 \text{ nm}$ ) on the surface of the titanium. Step (4) Thermal annealing in air at  $750 \text{ }^\circ\text{C}$ , for 1.5 h. Undoped samples were prepared according to steps 1, 3 and 4, thus avoiding step 2 (i.e. ion implantation).

value of Au (5 nm) was confirmed by Rutherford backscattering spectrometry (RBS) measurements using a 2.0 MeV  $\text{He}^+$  beam. Thus, the samples were inserted into a muffle and  $\text{TiO}_2$  NW synthesis was performed in air at  $750 \text{ }^\circ\text{C}$ , for 1.5 h (step 4). Gold nanoparticles form due to a de-wetting process and at  $750 \text{ }^\circ\text{C}$  catalyse the growth of the nanowire; the procedure of the NWs synthesis was optimized as reported in our previous works [15, 24, 30]. Samples synthesized, as described, are hereafter called “ $\text{TiO}_2$  NWs” or simply “NWs”.

## Doped NWs

Similarly to what was described in the previous paragraph, doped materials were synthesized by adding a further step (i.e. step 2) in the procedure described in Fig. 1. Step 2 consisted of the ion implantation of the titanium film. The titanium films were implanted with  $\text{Fe}^+$  or  $\text{Cr}^+$  ions at an energy of 150 keV for  $\text{Fe}^+$  (projected range  $\sim 83 \text{ nm}$ ) and 240 keV for  $\text{Cr}^+$  (projected range  $\sim 137 \text{ nm}$ ). Fluence ranged between  $3.4 \times 10^{15}$  and  $1.8 \times 10^{16} \text{ ion/cm}^2$ . Gold layer deposition (step 3) and annealing in air (step 4) were performed similarly to the un-implanted samples. Doped samples will be called by indicating the element (Fe or Cr) and the fluence, such as “Fe 1.8E16”.

## Electrolytes

The electrolytes used in the photo-electrochemical measurements are PBS (phosphate buffer solution)

100 mM,  $\text{pH} = 7.4$ . The resistivity of the solution is measured to be  $71 \Omega \cdot \text{cm}$  (conductivity  $1.4 \times 10^{-2} \text{ S/cm}$ ).

Scanning electron microscopy (SEM) analyses were performed by a Gemini field emission SUPRA 25 Carl Zeiss microscope operating at 3–5 kV. The total reflectivity measurements were obtained by using a Lambda 40 Perking-Elmer spectrophotometer. The band gap of the synthesized NWs was calculated using the Kubelka–Munk and Tauc-plot procedure [31]. Raman spectroscopy was carried out by using a micro-Raman Horiba Jobin Yvon HR800 system equipped with a 325 nm HeCd laser, emitted light was dispersed by 1800 grooves/mm kinematic grating with a 0.2 cm resolution. The power of the laser was kept between 1 and 10 mW and an objective of  $40\times$  with 0.75 NA has been used. X-ray diffraction (XRD) analyses are performed with a Rigaku Smartlab diffractometer equipped with a rotating anode of Cu  $\text{K}\alpha$  radiation operating at 45 kV and 200 mA, in grazing incidence mode at  $0.5^\circ$ , and  $\theta$ – $2\theta$  from  $20^\circ$  to  $60^\circ$ . The X-ray photoelectron spectroscopy (XPS) analyses were performed with a PHI 5000 versa probe instrument equipped with a monochromatic Al  $\text{K}\alpha$  X-ray source. The analyses were performed at a photoelectron take-off angle of  $45^\circ$  (relative to the sample surface). The XPS binding energy (B.E.) scale was calibrated on the Au  $4f_{7/2}$  peak at 84.0 eV. The electrochemical cell is customized and was realized with a 3D printer Raise3D Pro2 Plus (see Fig. 1a S.I.). It allocates a screen-printed electrode with a

quasi-reference electrode of Ag/AgCl and a gold dot as the counter electrode. The working electrode was realized by covering the sample with an inert polyolefinic film having a hole of 0.5 cm in diameter and an area of 0.2 cm<sup>2</sup>. The electrolyte volume in the cell is about 20 ml. A schematic diagram of photoelectric setup is reported in Fig. 1b S.I. The UV light used for photoelectrochemical experiments has a wavelength of 365 nm and an intensity of 10 mW/cm<sup>2</sup>. Linear sweep voltammetry (LSV) and electrochemical impedance spectroscopy (EIS) were acquired with a Versastat-4 potentiostat in a three-electrode setup [32, 33]. LSV was acquired by scanning from negative ( $-1.5 V_{\text{RHE}}$ ) to positive potentials ( $2 V_{\text{RHE}}$ ) at a scan rate of 5 mV/s; cyclic voltammetry (CV) was performed with a scan rate of 100 mV/sec.  $V_{\text{OC}}$  were performed waiting for 3 h for equilibration. EIS data were gathered using a 10 mV amplitude perturbation and a frequency between 0.1 and 10<sup>5</sup> Hz scanning 6 orders of magnitude and the data were processed with the Zviewer software. The potential is converted to the reversible hydrogen electrode (RHE) according to the equation:  $E_{\text{RHE}} = E_{\text{reference}} + 0.059 \cdot \text{pH} + 0.106 \text{ V}$ .

## Results

### Structural and optical characterization

The morphology and the crystalline structure of the NWs were studied by SEM, Raman and XRD analyses. In Fig. 2, a SEM micrograph of the nanomaterial is shown. The sample surface is covered by TiO<sub>2</sub> nanowires with a density of  $5 \times 10^8$  NWs/cm<sup>2</sup> (as calculated by the ImageJ software). Some main

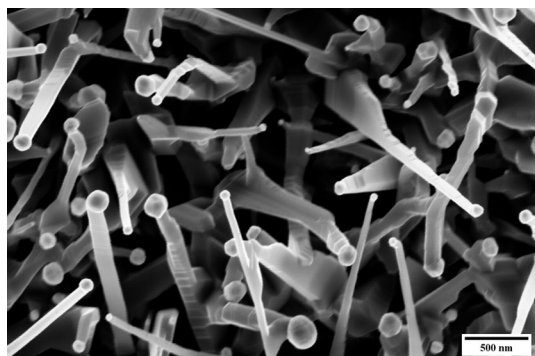


**Figure 2** SEM plan view of the surface of the NWs.

peculiarities can be observed in this image: 1) the NWs are faceted, pointing to a crystalline structure, 2) the NWs show an almost random orientation, and 3) the NWs have Au nanoparticles on the top. The length of the NWs is about 1–2 μm and the diameter of the nanowire (and of the Au NPs) ranges from 50 to 150 nm [14, 22, 23]. Doped and undoped samples (not shown here) present the same morphology. In Fig. 2 S.I. the Raman spectra for doped and undoped samples are shown. Even in this case, the Raman spectra of doped and undoped materials are indistinguishable. Raman showed the presence of two main peaks  $A_{1g}$  and  $E_g$ , related to the presence of the Rutile phase, while no Anatase phase is detectable [34]. The Rutile phase was reasonably formed at 750 °C annealing temperature. It is worth noting that the UV light source used for the Raman measurements has a penetration depth of about ~35 nm at  $\lambda = 325$  nm (considering an absorption coefficient of TiO<sub>2</sub> of  $2.9 \times 10^5 \text{ cm}^{-1}$  of the laser wavelength [31]), thus only the NWs contributed to the signal. Even the XRD patterns, shown in Fig. 3 S.I., showed the presence of the Rutile phase. In this figure, the black squared and the red circular dots indicate the position of the Rutile and Au peaks, respectively. In particular, the Bragg reflection peaks at 27.5°, 36.1°, 39.2°, 41.2°, 54.3° and 56.7° corresponding to (110), (101), (200), (111), (211) and (220) planes are apparent [PDF Card No.: 00-083-2242]. A careful investigation of the peak position of the doped and undoped samples indicated that they are un-shifted. The Au peaks due to the Au-NPs on top of the TiO<sub>2</sub> NWs are also apparent at 38.2°, 44.4° and 64.6° for (111), (200) and (220) planes, respectively [JCPDS Card No. 04-0784]. Despite the similarity of the SEM, Raman and XRD analyses, the reflectivity spectra in the UV–vis region and the XPS spectra present differences between the doped and undoped NWs. In Fig. 3a, we showed the absorption ( $A\% = 100 - R\%$ ) spectra for samples irradiated with different ions ( $\text{Fe}^+$  and  $\text{Cr}^+$ ) and fluencies. Figure 3a reports the undoped material with a black line, while the doped materials are represented by symbols. The figure indicates a higher absorbance in the visible due to the doping. An accurate analysis of the spectra of Fig. 3a was performed by using a method described elsewhere (by using a Kubelka–Munk and Tauc-plot procedure) [35, 36]. It indicates a decrease in the adsorption edge from  $402 \pm 4$  to  $437 \pm 4$  nm (meaning, in photon energy, from 3.08 to 2.83 eV). The results of this analysis are reported in Fig. 3b. It is worth noting that iron ions



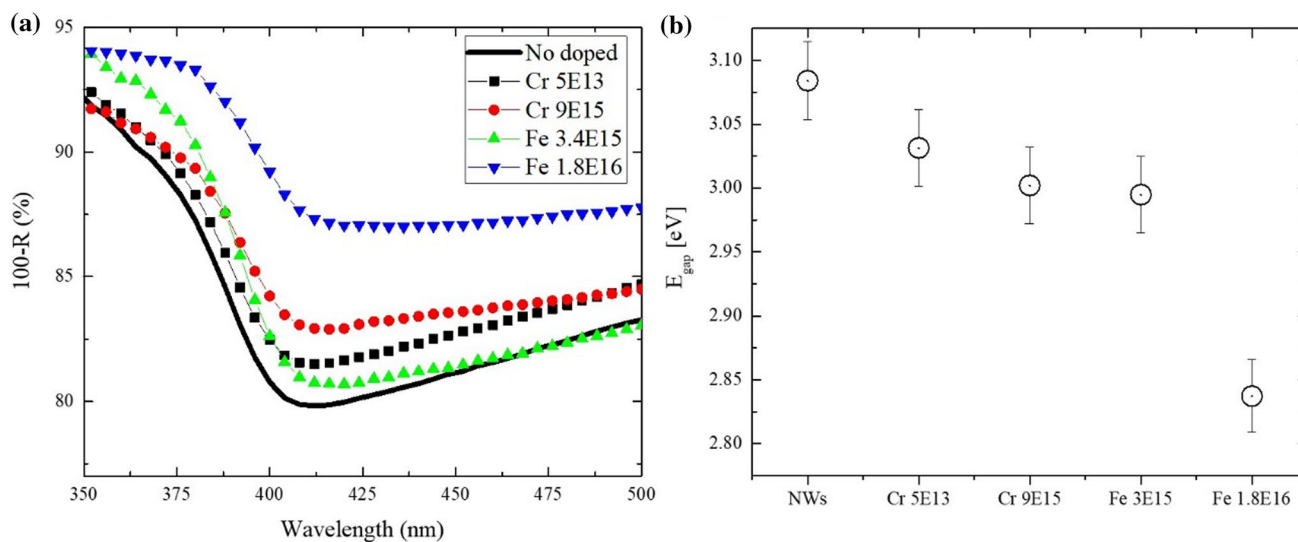


**Figure 3** **a** Absorbance ( $A\% = 100 - R\%$ ) spectra for NWs irradiated with different fluencies and ions (Fe and Cr). **b**  $E_g$  obtained by using a Kubelka–Munk and Tauc-plot procedure.

are more effective than chromium in reducing the optical band-gap of  $\text{TiO}_2$  indeed the sample irradiated with Cr, “Cr 9E15”, is less shifted than the sample “Fe 3.4E15” despite the higher dose of the former. In order to gain a deeper insight into the surface composition of the iron-doped  $\text{TiO}_2$  NWs (sample “Fe 1.8E16”), XPS analysis was performed. The survey spectrum shows intense peaks due to the presence of titanium and oxygen (see Fig. 4 S.I.). Carbon contamination is also detected. The presence of gold in the sample, due to the Au NPs on the NWs tips, is revealed by XPS at high-resolution (HR) and its atomic concentration

results to be of the order of 0.12%. The signal of  $\text{Au } 7/2,5/2$  is seen in the inset of Fig. 4 S.I. The diagnostic HR-XPS regions related to the Ti  $2p$ , O  $1s$  and Fe  $2p$  of the iron-doped NWs are shown in Fig. 4. The titanium signal consists of a spin–orbit doublet with the Ti  $2p_{3/2}$  component centred at 458.6 eV, consistent with the occurrence of titanium in the (IV) state [37]. The O  $1s$  region shows a band with a main component at 529.8 eV associated with the metal oxide species and a lower band centred at 531.8 eV which can be attributed mainly to the presence of hydroxyl groups on the surfaces ( $-\text{OH}$ ) [37, 38]. The ratio between the areas

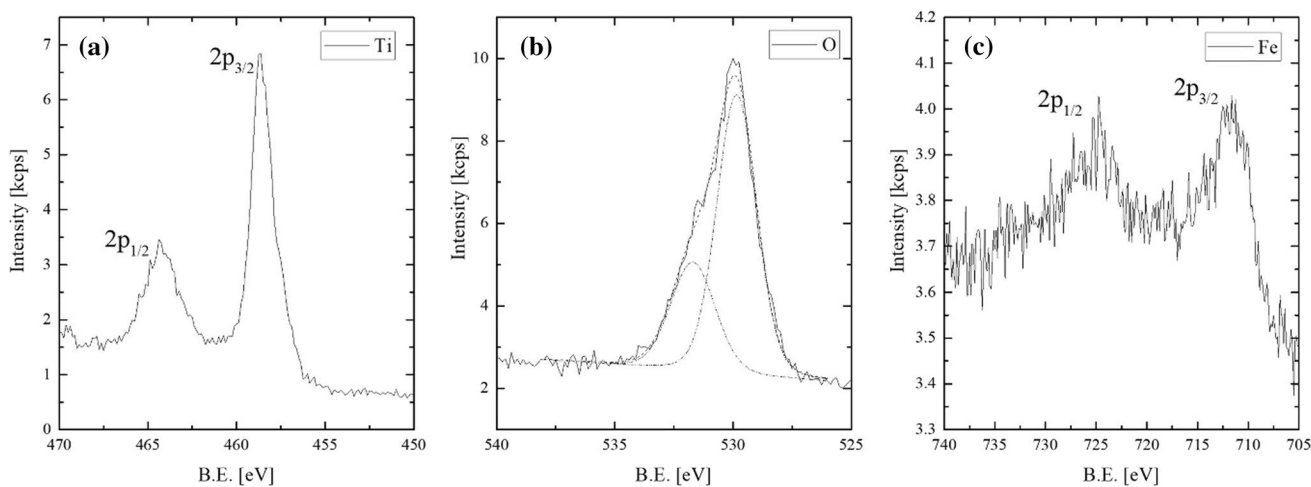


**Figure 4** High-resolution XPS spectra as obtained from the iron-doped  $\text{TiO}_2$  NWs in the **a** Ti  $2p$ , **b** O  $1s$  and **c** Fe  $2p$  regions.

of these two contributions is about 3:2. With regard to the dopant, the high-resolution XPS acquisition in the Fe 2*p* region, clearly indicates the presence of iron on the surface of the NWs. The signal related to the Fe 2*p* has the 2*p*<sub>3/2</sub> component centred at 711.6 eV, which is ascribable to the presence of Fe (III) in oxy/hydroxide species [39]. The atomic concentration of iron detected at the surface by XPS is 2.8%, to be compared with the 13.8% of titanium (see atomic concentrations in the table reported in Fig. 4 S.I.).

### Electrochemical characterization

Figure 5 reports the LSV curves of the undoped and “Fe 1.8E16” doped (called “undoped” and “doped” for brevity) samples in the dark and under UV illumination in the range between 0 and 1.2  $V_{RHE}$ . In this interval, the splitting of water is avoided. In the dark, the current is quite constant and very low: of the order of  $10^5$  and  $10^6$  A for undoped and doped samples, respectively. On the other hand, under UV light the photocurrent is observed. The points (square, circles and triangles) represent the open circuit voltages ( $V_{OC}$ ) in the dark and under illumination. These values are extracted from the chrono-potentiometric measurements shown in Fig. 5 S.I. The small vertical lines associated with the red and blue curves in Fig. 5 represent the position of

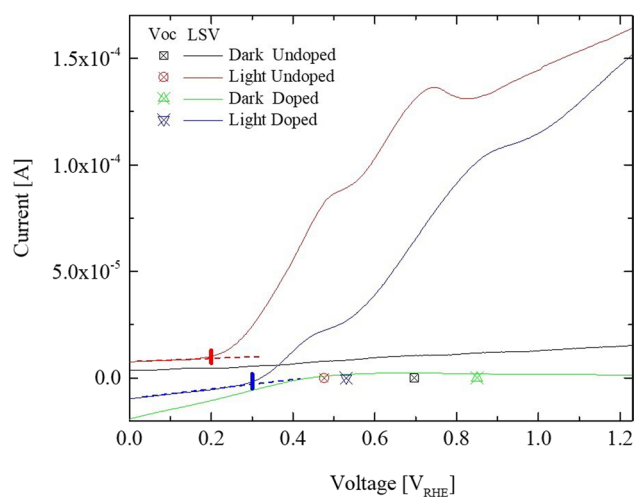


**Figure 5** LSV of the electrolytic-NWs junction for undoped and “Fe 1.8E16” sample in the dark and under UV illumination. The points (square, circle and triangles) represent the open circuit voltages ( $V_{OC}$ ) in the dark and under illumination, while vertical lines (red and blue) are the “onset potential” for undoped and doped NWs, respectively.

the “onset potential” i.e. the potential at which the photocurrent becomes measurable i.e. 0.2 and 0.3  $V_{RHE}$  for undoped and doped samples, respectively.  $V_{oc}$  in dark and  $V_{onset}$  are reported in Table 1. In Fig. 6a and b we reported, as an example, the measured impedance of the system: the real ( $Z'$ ) and imaginary ( $Z''$ ) parts of the impedance of the electrolytic-NWs junction for the undoped (Fig. 6a) and doped (Fig. 6b) as a function of frequency. It has been measured at a potential of 1  $V_{RHE}$  to make the light effect evident. The frequencies span 5 orders of magnitude, and two different behaviours can be observed for frequencies higher or lower than a “cut-off” frequency. This is 10 Hz and 100 Hz for undoped and doped samples, respectively, and it is represented in Fig. 6a and b as dashed vertical lines. These values are an intensity-related quantity and will be discussed later. For high frequency ( $\nu > \text{cut-off}$ ), the imaginary part of the impedance is negligible compared to the real part for both undoped and doped samples, thus the materials, in this frequency range, can be modelled as pure resistors. On the contrary, for frequencies lower than the cut-off frequency, the real and imaginary parts of the impedance have the same order of magnitude and must be analysed together. A parallel of a resistance and a capacitance can model the system. So, for all the frequencies, the system can be modelled as a resistor (related to the high-frequency response of the system) in series with a parallel of resistance ( $R$ )

**Table 1** Summary of electrochemical data for undoped and Fe-doped  $TiO_2$  NWs

	Undoped	Fe doped	
$V_{OC}$	0.70	0.85	$V_{RHE}$
$R_{\infty}$	400	1500	$\Omega$
Differential resistance	50	400	$K\Omega$
$V_{FB \text{ Dark}}$	0.21	0.32	$V_{RHE}$
Barrier height $\phi$	$0.50 \pm 0.05$	$0.53 \pm 0.05$	V
	$0.49 \pm 0.05$	$0.55 \pm 0.05$	
$R$ in dark	40	300	$K\Omega$
$N_D^*$ , Eff. donor density	$10^{22}$	$10^{21}$	$Cm^{-3}$
$V_{ph}$ photovoltage	0.22	0.35	V
$V_{onset}$	0.20	0.30	$V_{RHE}$
Cut-off frequency	10	100	Hz
$R$ in light	7	7	$k\Omega$
$V_{Shift}$	0.11	0.30	V
Density of trap states at surface	$\sim 5E14$	$\sim 5E14$	$Cm^{-2}$

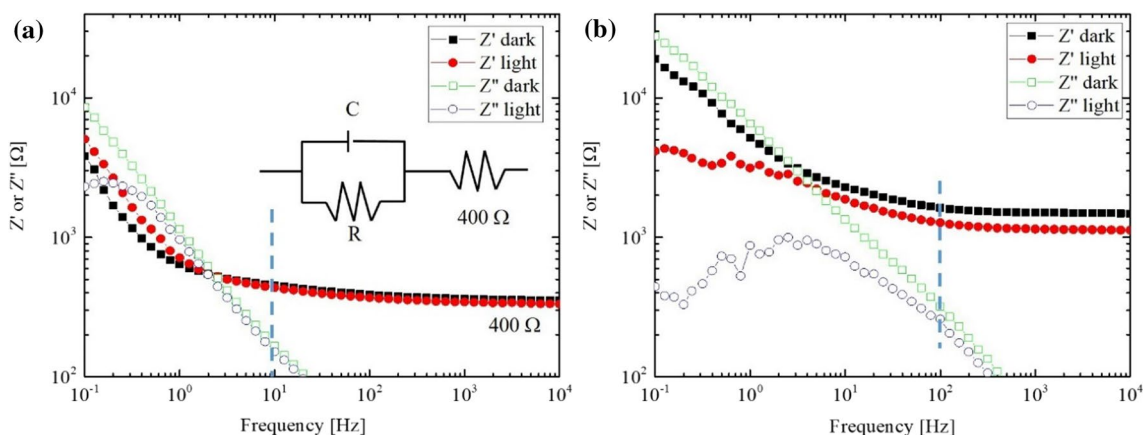


**Figure 6** The real ( $Z'$ ) and imaginary ( $Z''$ ) parts of the impedance of the electrolytic-NWs junction for the **a** undoped and **b** doped sample as a function of frequency. It is measured at a potential of  $1 V_{RHE}$  in dark and under UV-light illumination.

and capacitance ( $C$ ) as shown in Fig. 6a. This circuit is the well-known Randles circuit. Fitting the real and imaginary parts of the impedance allows the measure of the resistance  $R$  and capacitance  $C$  associated with the electrolytic-NWs junction.

We measured  $R$  and  $C$  at various potential values (from 0 to 1.2 V); in Fig. 7a and b, we reported the values of the resistance  $R$  as a function of the potential in the dark and under illumination for the undoped and doped samples. In Fig. 7c and d, we performed the Mott–Schottky plot (i.e. the inverse of the square of the capacitance as a function of the potential) for undoped and doped samples in the dark and under illumination.

## Discussion

Despite the negligible differences in the SEM, XRD and Raman results, the effect of the doping was recognized in the UV–Vis spectra. The reduction in the adsorption edge in the visible part of the spectra and the shift of the adsorption edge towards the visible wavelength were related to the presence of the dopant. Observing Fig. 3a, it is apparent that the Cr-induced modification of the spectra is less extensive than the effect of Fe doping. In particular, the reduction in the adsorption edge is lower for “Cr 9E15” than “Fe 3E15” despite the amount of Cr being higher than that of Fe. In any case, the largest effect of the doping can be observed for “Fe 1.8E16”. From these analyses, it is

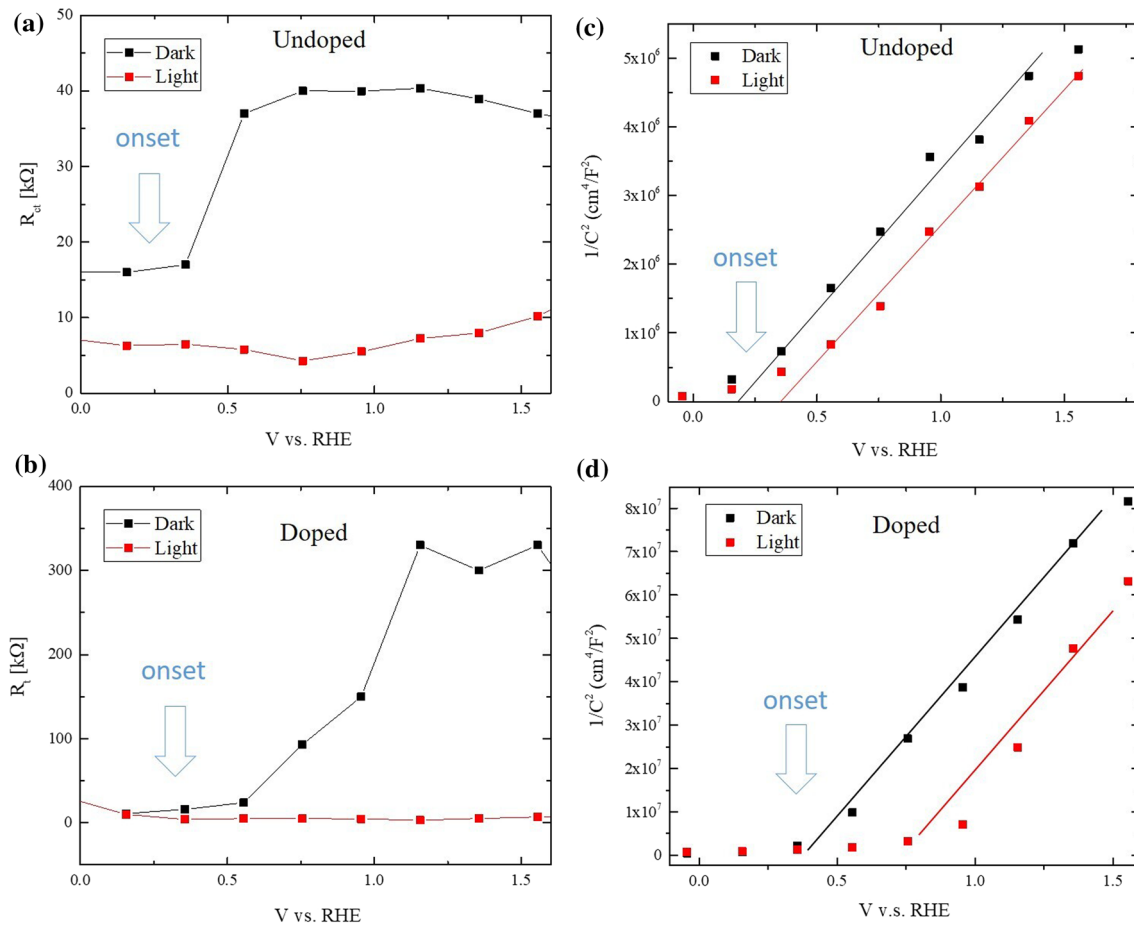
The “cut-off” frequency is drawn as a vertical dotted line. The Randles circuit is shown, reporting the equivalent resistance  $R$  and capacitance  $C$  associated with the electrolytic-NWs junction. The high-frequency resistance is also shown to be  $400 \Omega$ .

clear that the sample mostly modified by doping was the “Fe 1.8E16” sample. For this reason, in the present paper, we choose to show the electrochemical characterization of the undoped and “Fe 1.8E16” samples that we call for brevity, undoped and doped samples.

## Electrochemical behaviour

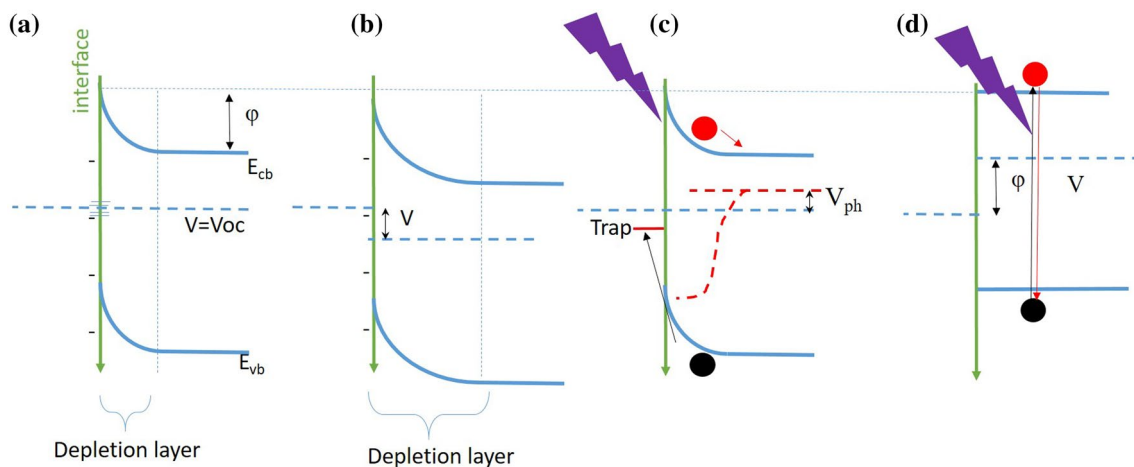
### Open circuit voltage

Figure 5 reports the  $V_{OC}$ , the LSV and the onset potential for the doped and undoped NWs under illumination and in the dark. Before critically analysing the LSV curves, it is worth recalling the physical interpretative paradigm for the description of the system in the dark and under illumination. Let’s first focus the attention on the undoped sample. We adopt the classical view, described in Fig. 8a, in which once the semiconductor is placed in contact with the liquid, charges are accumulated at the interface and a depletion layer is formed into the semiconductor. At equilibrium, the measured value of the  $V_{OC}$  in the dark (shown in Fig. 5, black square) is represented, in Fig. 8a, as the “position” of the Fermi level.  $V_{OC}$  values (compared to the reference electrode) in the dark, for doped (and undoped NWs), are shown in Table 1. Once we applied a potential to the interface, as shown in Fig. 8b, a potential drop applies to the depletion of the layer. The depletion layer thickness can be thus modulated and a change in the band bending occurs. Following the classical theory, the depth of the space



**Figure 7** Equivalent resistance  $R$  in the dark and under illumination as measured by fitting the experimental data with the Randles circuit associated with the electrolytic-NWs junction for **a** undoped and **b** doped samples. Mott–Schottky plots for **c**

undoped and **d** doped samples in the dark and under illumination. Linear fits are also reported. The “onset potential” is reported in both graphs.



**Figure 8** Semiconductor/electrolyte energy bands schematics. **a** Equilibrium configuration in the dark, **b** steady-state configuration in the dark: effect of the application of a potential

to the semiconductor, **c** steady-state under light illumination: effect of the light illumination on the semiconductor, and **d** steady state, flat-band condition configuration.



charge region  $W$  can be estimated by the following relation:

$$W = \sqrt{\frac{2\epsilon_0\epsilon_r(V_{sc} - V_{FB})}{qN_D^*}} \quad (1)$$

where  $V_{sc}$  is the voltage drop across the semiconductor,  $V_{FB}$  is the flat-band potential,  $N_D^*$  is the effective dopant density,  $\epsilon_0$  and  $\epsilon_r$  are the dielectric constants of the vacuum and the  $\text{TiO}_2$  ( $\epsilon_r \sim 100$  for Rutile [40]). As depicted from the above theoretical model, the current flowing in the dark can be due to both the presence of defects in the depletion layer and the capacitive effect related to the depletion layer. Nevertheless, the leakage current, flowing through the junction in dark, is very low: of the order of  $10^{-6}$  A or less. Moreover, from Fig. 5, it is possible to measure a differential resistance  $R = \frac{dV}{dI}$  for both samples that are of the order of 50 k $\Omega$  for undoped and 400 K $\Omega$  for the doped sample, as reported in Table 1. Once the semiconductor is illuminated, electron–hole couples are created. Holes are driven, by the band bending, to the surface and are transferred to the liquid allowing the oxidation of water molecules (or organic contaminants) while electrons are driven inside the material. Electrons, thus, are allowed to accumulate into the bulk making the  $V_{OC}$  more negative. The effect of illuminations is represented, in Fig. 8c, by the formation of a quasi-Fermi level for electrons and holes. Fermi levels (and quasi-Fermi levels) are represented by the dotted red curve that splits in two. The Fermi level of electrons (which are the majority carriers in  $\text{TiO}_2$ ), coincides with the  $V_{OC}$  and is thus measurable. The difference between the  $V_{OC}$  in the dark and under illumination is called photovoltage  $V_{ph}$  and it can be considered as a measure of the ability of the electrons to accumulate in the bulk. In our experiment, the  $V_{OC}$  is estimated to be 0.22 V for the undoped NWs and 0.35 V for Fe-doped NWs, as reported in Table 1. These results pointed out that doped NWs are able to accumulate more electrons than their undoped counterpart.

### Photocurrent

Holes, on the other side, are responsible for the photocurrent because they are transferred to the water medium (possibly through intra-gap trap states as shown in Fig. 8c).

Moreover, the photocurrent, measured as a function of the potential applied to the junction, is also reported in Fig. 5. From this figure, it is apparent the presence of a potential at which the photocurrent becomes non-negligible: the onset potential. The extrapolated “onset potential” is represented by a small vertical line approximately at 0.2  $V_{RHE}$  for the undoped NWs and 0.3  $V_{RHE}$  for Fe-doped material. These values can be correlated with the Schottky barrier height between the NWs and the liquid medium. Indeed, once the potential approaches the “onset potential”, the band are less and less bent until there is no more driving force for the transport of holes to the surface and the photocurrent is no longer influenced by the light illumination: at this potential, the photo-current becomes negligible. The situation is described in Fig. 8d in which the onset potential coincides with the flat band potential (as we will see in the next). From Fig. 8d, it is also clear that the difference between the onset potential and the  $V_{OC}$  in the dark is the barrier height of the junction  $\phi$ . The barrier height values for the un-doped and doped NWs values were reported in Table 1 and they are 0.50 and 0.55 V, respectively. These values are quite similar meaning that doping negligibly influences the charge at the interface.

### Electrochemical impedance spectroscopy

To gain more insight into the properties of the system, we performed EIS measurements. From these analyses, as described in the results section, we measured the real and imaginary parts of the impedance of the junction. Starting from the experimental considerations, we developed a simple physical model able to describe the system. From a schematic point of view, the samples can be divided into several zones: the bulk liquid, the Helmholtz layer, the interface (between nanowires and the gold nanoparticles), the depletion layer, and the bulk semiconductor. In the liquid, ions are allowed to transport current while in the semiconductor, majority and minority carriers work.

The majority carriers of the semiconductor, (in our case, the electrons) move with a time constant of the order of the dielectric relaxation time, i.e.  $10^{-12}$  s so they always follow the variation of measurement signal: in the timescale of  $1-10^{-4}$  s (corresponding to a frequency of  $1-10^4$  Hz of the EIS measurement), they are always in equilibrium (or in a steady-state if the

light is shed). Only the ions and minority carriers can contribute to EIS as a function of frequency.

Regarding the effect of the sinusoidal signal on the ion's motion in the liquid, we can, roughly, evaluate their contribution to the EIS spectra by evaluating their relaxation time ( $\tau = RC$ ). The capacitance of the Helmholtz layer can be considered as:

$$C = \frac{\epsilon_0 \epsilon_r A}{d} \quad (2)$$

where  $d$  is the peculiar distance between ions and surface and  $A$  is the area ( $0.2 \text{ cm}^2$  measured macroscopically). Considering the dielectric constants of the water  $\epsilon_r \sim 6$  [41] and ionic strength of  $0.1 \text{ M NaCl}$ ,  $d$  can be approximated by the Debye–Huckel length of the order of  $2.6 \text{ nm}$  and,  $C$  results approximately  $0.42 \text{ }\mu\text{F}$  ( $C/A = 2 \text{ }\mu\text{F}/\text{cm}^2$ ). The overall series resistance of the system is of the order of some hundreds of  $\Omega$  (as we will see later). So, the time constant  $RC$  related to the Helmholtz layer is  $0.2 \text{ ms}$  meaning a frequency of about  $5 \times 10^3 \text{ Hz}$ . We can consider this frequency, denoted in the next as  $f_H$ . The Helmholtz layer acts as a short circuit for frequencies higher than this value, while it acts as a capacitance for lower frequencies.

Let's now consider the effect of the frequency and light on the minority carrier of the  $\text{TiO}_2$  in the junction. For very high frequencies ( $f > f_{\text{cut-off}}$  and  $f > f_H$ ), the imaginary part of the impedance became negligible compared to the real part (refer to Fig. 6) regardless of the capacitance value. It is a common effect in the impedance spectra: for high frequencies, the junction capacitive contribution acts as a short-circuit and so the system behaves like a resistor. The high-frequency resistance  $R_\infty$  can be measured easily by extrapolating the value of the real part of the impedance at  $10^4 \text{ Hz}$ . In our case, it is  $400$  and  $1500 \text{ }\Omega$  for undoped and doped NWs and the values are reported in Table 1.

For low frequencies ( $f < f_{\text{cut-off}}$  and  $f < f_H$ ), the imaginary part of the impedance is comparable to the real part. Since the considerations reported in the Result section, we use the Randles circuit, reported in Fig. 6, to describe the impedance of the junction. Experimental data were fitted by the equivalent circuit for several potentials. The resistance  $R$  and capacitance  $C$  (plotted as a “Mott–Schottky” plot) were reported in Fig. 7: the resistance in the dark is  $15 \text{ K}\Omega$  at potentials lower than the onset potential but once the junction is polarized in “depletion” (i.e. the potential overcomes positively the onset potential), it becomes constant of

about  $40 \text{ K}\Omega$  for undoped NWs and  $300 \text{ K}\Omega$  for doped NWs, as reported in Table 1. The Mott–Schottky plot of Fig. 7 showed that the capacitance follows a linear trend that resembles the well-known equation [42]:

$$\frac{1}{C^2} = \frac{2}{q\epsilon_0\epsilon_r N_D^*} (V_{\text{sc}} - V_{\text{FB}}) \quad (3)$$

The calculated values of  $V_{\text{FB}}$  and  $N_D^*$  were reported in Table 1. Although this equation fits the experimental data, some considerations are needed. This equation came out by merging Eq. 1 and Eq. 2 and implies the validity of both equations. None of the conditions for the validity of these formulae is matched a priori: formulae 1 and 3 refer to a uniform, flat and not-nanostructured surface where the voltage drops only on the depletion layer, while the system under investigation, has a complex nanostructured surface with gold nanoparticles on the top of the nanowires and a non-negligible value of Helmholtz capacitance. Thus, the absolute value  $Nd^*$  should be corrected for the actual geometry we are working with. We can also consider that the presence of a non-negligible value of Helmholtz capacitance can influence the slope of the curve and alter the value of  $N_D^*$  [42] thus, to give a reliable donor concentration value, this formula should be modified. Despite it all, we noted that the obtained  $V_{\text{FB}}$  is very similar to the  $V_{\text{onset}}$  observed in Fig. 5 and the calculation of the barrier height led to reasonable values:  $0.5 \pm 0.05$  and  $0.55 \pm 0.05 \text{ eV}$  for undoped and doped NWs, respectively (as reported in Table 1). Also, the value of  $N_D^*$  deserves attention indeed we measured  $10^{22}$  and  $10^{21} \text{ cm}^{-3}$  for undoped and doped NWs. These concentrations, especially for the undoped material, are quite large. Nevertheless, we observed that the change in the values of the  $N_D^*$  between doped and undoped NWs is compatible with the change in the resistance ( $R$ ) values observed in EIS and the differential resistance observed in LSV. We found that these values for doped and undoped NWs differ by an order of magnitude from the values of  $N_D^*$ . This fact corroborates the idea that these quantities are correlated, as usual, with the doping concentration and the resistivity. Although the physical meaning of the absolute value of  $N_D^*$  should be revisited according to the real geometry, we believe that the relative value can give information on the doping of the NWs. To describe the EIS behaviour of the NWs during illumination, we need to recall

some basic concepts regarding the behaviour of a junction at very low frequencies ( $f < f_{\text{cut-off}}$ ). At sufficiently low frequencies, both the effect of ions in the liquid becomes important and the minority carriers of the NWs are able to follow the variation of the signal. In particular, the minority carrier's trap state concentration can be considered able to reach the equilibrium for these low frequencies even inside the depletion layer. However, the minority carrier concentration in the depletion layer is negligible and in order to reach the steady state configuration, they must be generated into (or removed from) the depletion layer. This means that the minority carriers can contribute to the capacitance in a timescale that depends on their generation rate [43]. Thus, electrical characteristics,  $R$  and  $C$ , measured following such a slow bias change, can depend on both the rates of the bias change (signal frequency) and the rate by which the charge within the semiconductor can be generated or removed (generation rate). In summary, the value of  $R$  and  $C$  can depend on the recombination and/or generation rate of the minority carrier. This effect is particularly evident when the semiconductor is illuminated. Indeed, when illuminated, the generation rate of minority carriers (holes) is faster, and the steady state condition for minority carriers can be reached even for higher signal frequencies. This fact changes the shape of both the real and the imaginary part of impedance also changing the relaxation time (and the equivalent  $R$  and  $C$ ). This effect can be observed until a cut-off frequency is reached (i.e. for  $f < f_{\text{cut-off}}$ ) over which the minority density is “freeze in”. Beyond the cut-off frequency, the illumination has a negligible effect on the EIS. The value of the cut-off depends on the illumination intensity and in our case, it is 10 and 100 Hz for undoped and doped material, respectively, as reported in Table 1.

Let's consider now the experimental data for frequencies lower than the  $f_{\text{cut-off}}$ . Under illumination, the equivalent resistance falls to 7 kΩ for both doped and undoped NWs as reported in Table 1. The resistance decreased because of the presence of minority photocarriers in the depletion layer. It adds a further independent channel for charge flow. The equivalent circuit can be considered thus constituted by two resistances in parallel:  $R$  in dark and light-induced  $R_L$ , as shown schematically in Fig. 6 S.I. As earlier described, at low frequencies, the system was able to rearrange the charges in a steady-state configuration. It could also allow the trap states,

lying at the interface, to be filled by photocarriers, so the capacitance changes due to the presence of filled trap states at the interface. We can consider the formation of a surface state capacitance in parallel with the capacitance measured in the dark. The mathematical expression for this capacitance should be [40]:

$$C_{\text{ss}} = N_{\text{ss}} \frac{q^2}{KT} f_{\text{ss}} (1 - f_{\text{ss}}) \tag{4}$$

where  $N_{\text{ss}}$  is the surface density of the surface states, and  $f_{\text{ss}}$  the fractional occupancy of the state that is due to the kinetics of the process [40]. This expression has been applied over many years, especially using an inert electrolyte that blocks the current flow [44, 45]. According to the previous considerations, the equivalent circuit used for describing the system is chosen formally identical to the model used in the dark (Fig. 6), but considering two capacitances ( $C$  and  $C_{\text{ss}}$ ) and two resistances ( $R$  and  $R_L$ ) in parallel to each other. The Mott–Schottky plot for the illuminated sample shows a shift in the  $V_{\text{FB}}$  of 0.1 V and 0.39 V for undoped and doped NWs, while the linear dependence is maintained even if small modifications of the slope are observed (refer to Fig. 7c and d). This shift can be attributed to charges accumulated at the interface between the semiconductor and the liquid. It is positive, meaning that the surface states are positive too and thus due to the accumulation of photo-holes. The density of charges  $Q_{\text{ss}}$  due to the surface states filled by the photocarrier can be estimated:

$$\text{Density of trap} = \frac{\Delta C \Delta V}{e} \tag{5}$$

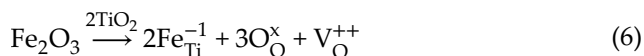
where  $\Delta C$  and  $\Delta V$  are the capacitance (per unit surface) and the voltage difference between dark and illuminated. The values of the density of trap states filled during the illumination are reported in Table 1 and are about  $5 \times 10^{14} \text{ cm}^{-2}$  for both undoped and doped NWs.

### Final considerations

Some final considerations can be depicted from the values reported in Table 1. First of all, the barrier height for the doped and the undoped NWs are very similar meaning that doping has a small effect on the interface between liquid and semiconductor. Secondly, once illuminated, the density of trap states at the interface has the same values in both undoped and doped

NWs. This result suggests that: (1) the surface trap concentration due to doping is lower than the amount of surface trap states realized during the illumination, and (2) the light introduces a similar accumulation of holes at trap interface states in doped and undoped NWs. It also means that the influence of doping on the interface between liquid and semiconductor is negligible even under illumination.

On the contrary, bulk quantities, such as  $R_{\infty}$ , differential resistance,  $R$  in the dark and  $N_D^*$ , have a quite large change with doping (in particular  $R$  in the dark and  $N_D^*$  changes of 1 order of magnitude). The interpretation is related to a decrease in major carrier concentration due to doping. Indeed, the introduction of a dopant  $Fe^{3+}$  into a  $TiO_2$  can lead to the substitution of the foreign atom into a Ti sub-lattice. The following Eqs. (6) and (7), expressed with the Kröger–Vink notation, describe two possible mechanisms for the compensation of the extra charge due to the introduction of  $Fe^{3+}$  into the  $TiO_2$  lattice:



Equation 6 leads to the formation of oxygen vacancies, while Eq. 7 to the formation of holes. Compensating effects related to Eq. 6 seem the most appropriate order to describe the effect of Fe doping in NWs for the above-described change in bulk quantities. On the other hand, the charge-compensating effect can lead to the formation of deep levels inside the bandgap, as was proposed for bulk Fe-doped  $TiO_2$  [46, 47].  $Fe^{3+}$  can thus introduce trap states inside the band gap that can decrease the position on the Fermi level and can reduce the concentration of free electrons by trapping electrons. The observed behaviour is compatible with Eq. 7 and with the formation of deep levels in the bulk of the nanowires that pin the Fermi level reducing the concentration of electrons in the bulk.

## Conclusion

In this paper, we report a study of electrical properties of  $TiO_2$  nanowires synthesized, by employing a seed-assisted technique. Making use of ion implantation technology, we were able to grow Cr- or Fe-doped NWs. The NWs showed peculiar properties: they are

crystalline and have Au nanoparticles on top. Structural analyses showed a good crystallinity of the NWs, which grow in the Rutile phase. The effect of Fe doping has been investigated by using LSV and EIS techniques. We measured the photovoltage and the barrier height of the semiconductor-electrolyte junction. We also evaluated the density of the hole trap states at the interface during the illumination. We clarified the role of doping in influencing the bulk of the material while having a negligible effect on the hole transfer process during illumination. On the contrary, the doping decreased the conductivity and the electron concentration by about one order of magnitude, leading the fact to a compensating effect.

## Acknowledgements

The authors would like to express their sincere gratitude to Giuseppe Pantè of CNR-IMM Catania, Italy, for his valuable assistance in solving the technical challenges and ensuring the smooth functioning of the laboratory facilities. The authors wish to thank Prof. G. Malandrino and Prof. G. Condorelli for their support in the XRD and XPS measurements. This work was partially supported by Bio-Nanotech Research and Innovation Tower grant BRIT PONa3\_00136, University of Catania, for the structural characterization with Smartlab diffractometer facility and XPS characterization with 5000 Versa probe X-ray photoelectron spectrometer.

## Author contributions

M. Zimbone contributed to conceptualization, methodology, formal analysis, investigation, data curation, writing—original draft, writing—review & editing. S. Battiato contributed to methodology, investigation, data curation, writing—review & editing. L. Calcagno contributed to formal analysis, writing—original draft, writing—review & editing. G. Pezzotti Escobar contributed to investigation. G. Pellegrino contributed to investigation, formal analysis, data curation. S. Mirabella contributed to Validation. F. Giuffrida contributed to formal analysis, data curation. G. Impellizzeri contributed to validation, supervision, funding. All authors have read and agreed to the published version of the manuscript.



## Funding

Open access funding provided by IMM - CATANIA C/O DIP. DI FISICA E ASTRONOMIA - UNIV. DEGLI STUDI DI CATANIA VIA SANTA SOFIA 64 within the CRUI-CARE Agreement. This work was partially funded by the European Union (NextGeneration EU), through the MUR-PNRR project SAMOTHRACE (ECS00000022).

## Data availability

Not applicable.

## Declarations

**Conflict of interest** All authors declare that there is no conflict of interest or competing interests.

**Ethical approval** Not applicable.

**Supplementary Information** The online version contains supplementary material available at <https://doi.org/10.1007/s10853-024-09763-6>.

**Open Access** This article is licensed under a Creative Commons Attribution 4.0 International License, which permits use, sharing, adaptation, distribution and reproduction in any medium or format, as long as you give appropriate credit to the original author(s) and the source, provide a link to the Creative Commons licence, and indicate if changes were made. The images or other third party material in this article are included in the article's Creative Commons licence, unless indicated otherwise in a credit line to the material. If material is not included in the article's Creative Commons licence and your intended use is not permitted by statutory regulation or exceeds the permitted use, you will need to obtain permission directly from the copyright holder. To view a copy of this licence, visit <http://creativecommons.org/licenses/by/4.0/>.

## References

- [1] Fujishima A, Zhang X, Tryk A (2008) TiO<sub>2</sub> photocatalysis and related surface phenomena. *Surf Sci Rep* 63:515–582
- [2] Natarajan TS, Tayade RJ, Bajaj HC (2009) Photocatalytic degradation of methylene blue dye using ultraviolet light emitting diodes. *Ind Eng Chem Res* 48:10262–10267
- [3] Zhang X, Tryk D, Irie H, Fujishima A (2023) Handbook of self-cleaning surfaces and materials. In: Fujishima A (ed) *From fundamentals to applications*. Wiley-CVH, New York, pp 1–736
- [4] Banerjee S, Dionysiou DD, Pillai SC (2015) Self-cleaning applications of TiO<sub>2</sub> by photo-induced hydrophilicity and photocatalysis. *Appl Catal B: Environ* 176–177:396–428
- [5] Zimbone M, Cacciato G, Boutinguiza M, Gulino A, Cantarella M, Privitera V, Grimaldi MG (2019) Hydrogenated black-TiOx: a facile and scalable synthesis for environmental water purification. *Catal Today* 321–322:146–157
- [6] Zimbone M, Cacciato G, Buccheri MA, Sanz R, Piluso N, Reitano R, LaVia F, Grimaldi MG, Privitera V (2016) Photocatalytic activity of amorphous hydrogenated TiO<sub>2</sub> obtained by pulsed laser ablation in liquid. *Mater Sci Semicond Process* 42:28–31
- [7] Zimbone M, Buccheri MA, Cacciato G, Sanz R, Rappazzo G, Boninelli S, Reitano R, Romano L, Privitera V, Grimaldi MG (2015) Photocatalytic and antibacterial activity of TiO<sub>2</sub> nanoparticles obtained by laser ablation in water. *Appl Catal B: Environ* 165:487–494
- [8] Sanz R, Romano L, Zimbone M, Buccheri MA, Scuderi V, Impellizzeri G, Scuderi M, Nicotra G, Jensen J, Privitera V (2015) UV-black rutile TiO<sub>2</sub>: an antireflective photocatalytic nanostructure. *J Appl Phys* 117(7):074903
- [9] Zimbone M, Cacciato G, Sanz R, Carles R, Gulino A, Privitera V, Grimaldi MG (2016) Black TiOx photocatalyst obtained by laser irradiation in water. *Catal Commun* 84(5):11–15
- [10] Irie H, Miyauchi M, Liu M, Qiu X, Yu H, Sunada K, Hashimoto K (2016) Visible-light-sensitive photocatalyst: nanocluster-grafted titanium dioxide for indoor environmental remediation. *J Phys Chem Lett* 7:75–84
- [11] Lee K, Yoon H, Ahn C, Park J, Jeon S (2019) Strategies to improve the photocatalytic activity of TiO<sub>2</sub>: 3D nanostructuring and heterostructuring with graphitic carbon nanomaterials. *Nanoscale* 11:7025–7040
- [12] Yashwanth HJ, Rondiya SR, Dzade NY, Hoyer RLZ, Choudhary RJ, Phase DM, Dhole SD, Hareesh K (2022) Improved photocatalytic activity of TiO<sub>2</sub> nanoparticles through nitrogen and phosphorus co-doped carbon quantum



- dots: an experimental and theoretical study. *Phys Chem Chem Phys* 24:15271–15279
- [13] Dorray M, Goh BT, Sairi NA, Woi PM, Basirun WJ (2018) Improved visible-light photocatalytic activity of TiO<sub>2</sub> co-doped with copper and iodine. *Appl Surf Sci* 439:999–1009
- [14] Alijani M, Kaleji BK, Rezaee S (2017) Improved visible light photocatalytic activity of TiO<sub>2</sub> nano powders with metal ions doping for glazed ceramic tiles. *Opt Quantum Electron* 49:1–13
- [15] Giuffrida F, Calcagno L, Leonardi AA, Cantarella M, Zimbone M, Impellizzeri G (2023) Enhancing the photocatalytic properties of doped TiO<sub>2</sub> nanowires grown by seed-assisted thermal oxidation. *Thin Solid Films* 771:13978
- [16] Etacheri V, Di Valentin C, Schneider J, Bahnemann D, Pillai SC (2015) Visible-light activation of TiO<sub>2</sub> photocatalysts: advances in theory and experiments. *J Photochem Photobiol C* 25:1–29
- [17] Floris F, Fornasari L, Bellani V, Marini A, Banfi F, Marabelli F, Beltrami F, Ercolani D, Battiato S, Sorba L, Rossella F (2019) Strong modulations of optical reflectance in tapered core-shell nanowires. *Materials* 12(21):3572
- [18] Battiato S, Wu S, Zannier V, Bertoni A, Goldoni G, Li A, Xiao S, Han XD, Beltram F, Sorba L (2019) Polychromatic emission in a wide energy range from InP-InAs-InP multi-shell nanowires. *Nanotechnology* 30:194004
- [19] Wu S, Peng J, Battiato S, Zannier V, Bertoni A, Goldoni G, Xie X, Yang J, Xiao S, Qian C, Song F, Song F, Sun S, Dang J, Yu Y, Beltram F, Sorba L, Li A, Li BB, Rossella F, Xu X (2019) Anisotropies of the g-factor tensor and diamagnetic coefficient in crystal-phase quantum dots in InP nanowires. *Nano Res* 12:2842–2848
- [20] Cao F, Xiong J, Wu F, Liu Q, Shi Z, Yu Y, Wang X, Li L (2016) Enhanced photoelectrochemical performances from rationally designed anatase /rutile TiO<sub>2</sub> heterostructures. *ACS Appl Mater Interfaces* 8(19):12239–12245
- [21] Aghaee M, Verheyen J, Stevens AAE, Kessels WMM, Creatore M (2019) TiO<sub>2</sub> thin film patterns prepared by chemical vapor deposition and atomic layer deposition using an atmospheric pressure microplasma. *Plasm Process Polym* 16(12):1900127
- [22] Hwang YJ, Hahn C, Liu B, Yang P (2012) Photoelectrochemical properties of TiO<sub>2</sub> nanowires array: a study of the dependence on length and atomic layer deposition coating. *ACS Nano* 6(6):5060–5069
- [23] Rahmat ST, Tan WK, Kawamura G, Matsuda A, Lockman Z (2020) Synthesis of rutile TiO<sub>2</sub> nanowires by thermal oxidation of titanium in the presence of KOH and their ability to photoreduce Cr(VI) ions. *J Alloys Compd* 812(5):152094
- [24] Arcadipane E, Sanz R, Amiard G, Boninelli S, Impellizzeri G, Privitera V, Bonkerud J, Bhoodoo C, Vines L, Svensson BG, Romano L (2016) Single-crystal TiO<sub>2</sub> nanowires by seed assisted thermal oxidation of Ti Foil: synthesis and photocatalytic properties. *RSC Adv* 6:55490–55498
- [25] Zimbone M, Cantarella M, Impellizzeri G, Battiato S, Calcagno L (2021) Synthesis and photochemical properties of monolithic tio2 nanowires diode. *Molecules* 26(12):3636
- [26] Sanzone G, Zimbone M, Cacciato G, Ruffino F, Carles R, Privitera V, Grimaldi MG (2018) Ag/TiO<sub>2</sub> nanocomposite for visible light-driven photocatalysis. *Superlattices Microstruct* 123:394–402
- [27] Zimbone M, Musumeci P, Baeri P, Messina E, Boninelli S, Compagnini G, Calcagno L (2012) Rotational dynamics of gold nanoparticle chains in water solution. *J Nanopart Res* 14(12):1–11
- [28] Zimbone M, Baeri P, Calcagno L, Musumeci P, Contino A, Barcellona ML, Bonaventura G (2014) Dynamic light scattering on bioconjugated laser generated gold nanoparticles. *PLoS ONE* 9(3):89048
- [29] Impellizzeri G, Scuderi V, Romano L, Sberna PM, Arcadipane E, Sanz R, Scuderi M, Nicotra G, Bayle M, Carles R, Simone F, Privitera V (2014) Fe ion-implanted TiO<sub>2</sub> thin film for efficient visible-light photocatalysis. *J Appl Phys* 116:173507
- [30] Arcadipane E, Sanz R, Miritello M, Impellizzeri G, Grimaldi MG, Privitera V, Romano L (2016) TiO<sub>2</sub> nanowires on Ti thin film for water purification. *Mater Sci Semicond Process* 42:24–27
- [31] Tanemura S, Miao L, Jin P, Kaneko K, Terai A, Nabatova-Gabain N (2003) Optical properties of polycrystalline and epitaxial anatase and rutile TiO<sub>2</sub> thin films by rf magnetron sputtering. *Appl Surf Sci* 212–213:654–660
- [32] Battiato S, Bruno L, Pellegrino AL, Terrasi A, Mirabella S (2023) Optimized electroless deposition of NiCoP electrocatalysts for enhanced water splitting. *Catal Today* 423:113929
- [33] Battiato S, Pellegrino AL, Pollicino A, Terrasi A, Mirabella S (2023) Composition-controlled chemical bath deposition of Fe-doped NiO microflowers for boosting oxygen evolution reaction. *Int J Hydrog Energy* 48(48):18291–18300
- [34] Frank O, Zikalova M, Laskova B, Kurti J, Koltai J, Kavan L (2012) Raman spectra of titanium dioxide (anatase, rutile) with identified oxygen isotopes (16, 17, 18). *Phys Chem Chem Phys* 14:14567–14572

- [35] Makuła P, Pacia M, Macyk W (2018) How to correctly determine the band gap energy of modified semiconductor photocatalysts based on UV–Vis spectra. *J Phys Chem Lett* 9(23):6814–6817
- [36] Tauc J (1974) Optical properties of amorphous semiconductors. In: *Amorphous and liquid semiconductors*. Springer, Plenum Press, New York, p 175
- [37] Sleigh C, Pijpers AP, Jaspers A, Coussens B, Meier RJ (1996) On the determination of atomic charge via ESCA including application to organometallics. *J Electron Spectrosc Relat Phenom* 77:41–57
- [38] Fan C, Chen C, Wang J, Fu X, Ren Z, Qian G, Wang Z (2015) Black hydroxylated titanium dioxide prepared via ultrasonication with enhanced photocatalytic activity. *Sci Rep* 5:11712
- [39] Suyantara GPW, Nurul RI, Ulmaszoda A, Miki H, Sasaki K (2023) Effect of goethite ( $\alpha$ -FeOOH) nanoparticles on the surface properties and flotation behavior of chalcopyrite. *J Environ Chem Eng* 11(3):110006
- [40] Parker RA (1961) Static dielectric constant of rutile (TiO<sub>2</sub>), 1.6–1060 K. *Phys Rev* 124:1719–1722
- [41] Rothenberger G, Fitzmaurice D, Graetzel M (1992) Spectroscopy of conduction band electrons in transparent metal oxide semiconductor films: optical determination of the flatband potential of colloidal titanium dioxide films. *J Phys Chem* 96(14):5983–5986
- [42] Hankin A, Bedoya-Lora FE, Alexander JC, Regoutz A, Kelsall GH (2019) Flat band potential determination: avoiding the pitfalls. *J Mater Chem A* 7:26162–26176
- [43] Klahr B, Gimenez S, Fabregat-Santiago F, Hamann T, Bisquert J (2012) Water oxidation at hematite photoelectrodes: the role of surface states. *J Am Chem Soc* 134:4294–4302
- [44] Frese KW, Morrison SR (1979) Electrochemical measurements of interface states at the GaAs/oxide interface. *J Electrochem Soc* 126:1235–1241
- [45] Scurtu R, Ionescu NI, Lazarescu M, Lazarescu V (2009) Surface states- and field-effects at *p*- and *n*-doped GaAs(111)A/solution interface. *Phys Chem Chem Phys* 11:1765–1770
- [46] Liu M, Qiu X, Miyauchi M, Hashimoto K (2013) Energy-level matching of Fe(III) ions grafted at surface and doped in bulk for efficient visible-light photocatalysts. *J Am Chem Soc* 135:10064–10072
- [47] Wen LP, Liu BS, Zhao XJ, Nakata K, Murakami T, Fujishima A (2012) Synthesis, characterization, and photocatalysis of Fe-doped TiO<sub>2</sub>: a combined experimental and theoretical study. *Int J Photoenergy* 2012:368750

**Publisher's Note** Springer Nature remains neutral with regard to jurisdictional claims in published maps and institutional affiliations.